



A COMPLEMENTARY NUMERICAL AND PHYSICAL INVESTIGATION OF VORTEX-INDUCED VIBRATION

H. M. BLACKBURN

*CSIRO Building Construction and Engineering, P.O. Box 56
Highett, VIC 3190, Australia*

R. N. GOVARDHAN AND C. H. K. WILLIAMSON

*Mechanical and Aerospace Engineering
Upson Hall, Cornell University, Ithaca, NY 14853, U.S.A.*

(Received 15 September 2000, and in final form 23 October 2000)

Results are presented from low Reynolds number experimental investigations of vortex-induced vibration and comparison is made with results from corresponding two- and three-dimensional direct numerical simulations. It is shown that three-dimensional simulations are required to reproduce the response envelope observed experimentally. Phase-averaged contours of span-wise vorticity demonstrate the presence of the 2P shedding mode on the lower response branch in both the experimental and three-dimensional simulation results.

© 2001 Academic Press

1. INTRODUCTION

A NUMBER OF FUNDAMENTAL STUDIES of the vortex-induced vibration of slender cylindrical structures in cross flow have been published over the last decade. Recent experiments [e.g., Khalak & Williamson (1999)] have extended the early works, such as that of Feng (1968), while numerical simulations have also started to make inroads at the lower end of the Reynolds number spectrum. Despite the quantity of experimental and numerical activity, there has been no published study in which it has been attempted to match parameters between the two domains. In this work, our aim is to increase understanding of the problem by comparing results from water-tunnel experiments with those from two- and three-dimensional direct numerical simulations, in which Reynolds numbers and mechanical dynamic parameters such as cylinder mass and damping ratios are the same for both the experiments and the simulations.

2. EXPERIMENTAL METHOD

Figure 1 shows a diagram of the experimental equipment. The set-up uses a cylinder that is cantilevered from an air-bearing sled through a bi-axial force transducer. A position transducer is attached to the sled, and a spring suspension system provides central restoring forces to the cylinder–sled assembly. The bearings are mounted above a water channel; the cylinder pierces the water surface and can translate cross-flow on its bearings. The free end of the cylinder had an end plate located close to the lower wall of the water channel. DPIV measurements of two components of the velocity field can be obtained using laser-sheet

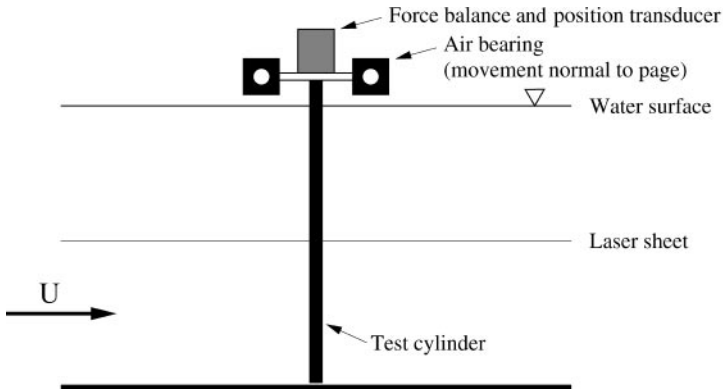


Figure 1. Diagram of experimental set-up in water tunnel working section.

lighting that is parallel to the water surface, and image capture can be conditioned on cylinder position. More detailed descriptions of the experimental apparatus may be found in Khalak & Williamson (1997) and Govardhan & Williamson (2000).

In running the experiments, the cylinder, spring rate and damping were kept constant, and the reduced velocity was varied by changing the flow speed, hence the Reynolds number varied with reduced velocity. The submerged depth of the cylinder had an aspect ratio (length/diameter) of $L/D = 26.7:1$. The cylinder mass ratio $m^* = 4m/\rho\pi D^2 = 50.8$, where m is the sprung mass per unit length of submerged cylinder depth, and ρ is the density of water. The damping ratio, derived from the free-vibration decay rate in air, $\zeta = 0.0024$, giving a mass-damping parameter $m^*\zeta = 0.122$ (cf. Feng 1968, where $m^*\zeta \approx 0.25$). A reference Reynolds number is $Re = UD/\nu = 556$ at a reduced velocity $V_r = UT_n/D = 5.00$, where U is the average free-stream flow speed, T_n is the free-vibration natural frequency in air and ν is the kinematic viscosity of water.

Although good response amplitude data could be obtained, difficulty was experienced in obtaining reliable force and DPIV measurements at the Reynolds numbers used in these experiments. For purposes of comparison with the three-dimensional simulation results, we have included force and vorticity data obtained at somewhat higher Reynolds numbers ($Re \approx 1250$ at peak response amplitude) and mass damping ($m^*\zeta = 0.251$, similar to that used by Feng), as described in more detail in Govardhan & William (2000, 2001).

3. SIMULATION METHOD

The simulation method and its numerical implementation using a spectral element–Fourier spatial discretisation has been previously documented in Blackburn & Karniadakis (1993) and Blackburn & Henderson (1996, 1999). The incompressible Navier–Stokes equations are solved in an accelerating reference frame, and this simulation is coupled to that for a set of first-order ODEs that describe the motion of the cylinder in response to the forces exerted on it by the fluid. The reference frame acceleration, and velocity boundary conditions on the outer edge of the flow domain, are set according to the values obtained by simulating the response of the cylinder. This method allows simulation of the rigid-body response of a freely oscillating cylinder without the overheads associated with distortion of the mesh to accommodate motion of the cylinder within the domain.

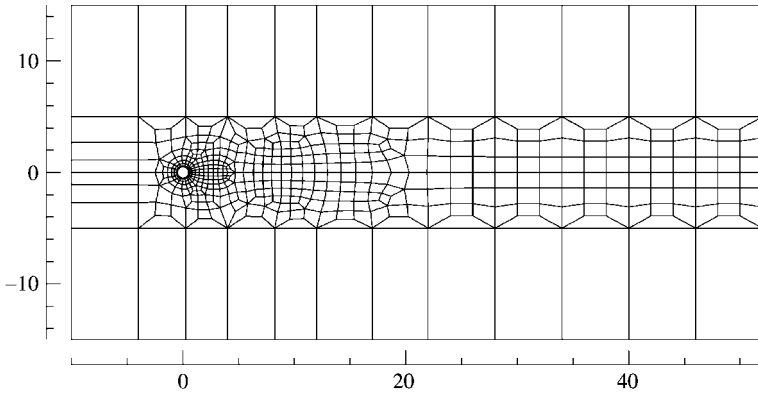


Figure 2. Computational mesh, showing element boundaries; dimensions are based on cylinder diameter.

The computational mesh is shown in Figure 2. For three-dimensional simulations, Fourier expansions are used in the cylinder-axis direction; the two-dimensional projection of the three-dimensional mesh is identical to that used for the two-dimensional simulations. The mesh shown has 502 elements, and 10th-order Gauss–Lobatto–Legendre-based two-dimensional Lagrange shape functions were used for the in-plane spatial discretization. This was found to be adequate for 4-figure convergence of integral measures of the two-dimensional simulation results [see the similar and related tests presented in Blackburn & Henderson (1999)]. The dynamic equations are integrated in time using a second-order operator-splitting scheme.

For all the results presented here, the axial extent of the three-dimensional domain was $3.28D$, with 24 planes of data. While the axial extent and resolution are both lower than desirable, the size was limited by computer memory and simulation time constraints. The three-dimensional simulations required approximately 2 GB of memory and 12 CPU-hours per motion cycle when run on an NEC SX-4 computer (peak speed approximately 2 GFLOPS/processor). Typical runs used 4–6 CPUs.

Reynolds numbers and dimensionless dynamic parameters in the simulations were chosen to match those in the experimental set-up, as described in Section 2. It should be noted that, even with this degree of matching, cylinder-end boundary conditions differ between the experiments and the simulations, since with the adoption of Fourier expansions the flow is assumed periodic in the axial direction for the simulations.

4. RESPONSE AMPLITUDE RESULTS

A compilation of experimental and simulated cross-flow response amplitudes is presented in Figure 3. The average peak dimensionless amplitude $A^* = \bar{y}_{\max}/D$, while the reduced velocity $V_r = UT_n/D$ is normalized by an appropriate representative Strouhal number for a fixed cylinder $St = f_v D/U$ to form StV_r . This normalization of reduced velocities has been carried out because of the disparity of two- and three-dimensional Strouhal numbers at these Reynolds numbers: for the two-dimensional results, $St = 0.225$ (Blackburn & Henderson 1999), while for both the simulated three-dimensional and experimental results, $St = 0.205$, where both values are appropriate for a Reynolds number $Re \sim 500$ (Norberg 1994).

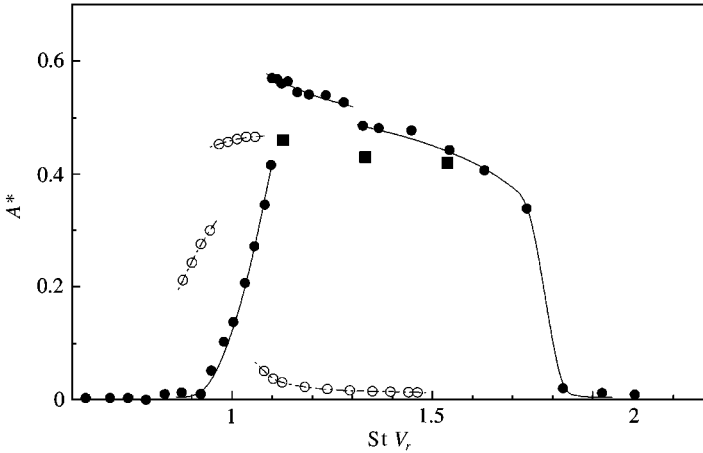


Figure 3. Dimensionless average peak response amplitude A^* as a function of StV_r : ●, experimental results; ■, three-dimensional simulations; ○, two-dimensional simulations.

4.1. EXPERIMENTAL

Turning first to the experimental results, the response envelope exhibits three distinct branches, similar to results previously presented for higher Reynolds numbers and lower mass-damping values by Khalak & Williamson (1997, 1999). The two highest amplitude branches, the “upper” and “lower” branches here are less separated in amplitude than for the previous results, which is thought likely to be a result both of Reynolds number and mass-damping effects.

4.2. THREE-DIMENSIONAL SIMULATIONS

The three-dimensional simulations were carried out for reduced velocities chosen to place them near the highest observed amplitudes on the upper and lower response branches ($StV_r = 1.13, 1.33$ and 1.58). The response amplitudes, while similar to the experimental results, are somewhat smaller, which is thought likely to be a consequence of the restricted axial periodic length of the computational domain ($3.28D$), and, less significantly, to the differences in end conditions. The difference in amplitudes for the three values of StV_r does, however, mimic the experimentally observed behaviour, with the highest amplitude occurring at the lowest reduced velocity.

4.3. TWO-DIMENSIONAL SIMULATIONS

Given the high demand on computer resources made by the three-dimensional simulations, it is obviously of interest to compare the results for the two-dimensional simulations with the experiments and the three-dimensional simulations. The two-dimensional results were obtained using small decrements of U between each run. It is apparent from an examination of Figure 3 that, although the peak response observed for the two-dimensional simulations is similar to the higher of the three-dimensional results, the computed results are substantially different from the experimental measurements in terms of the StV_r location and extent of the peak response branch. It is interesting to note that the general form and position of the response amplitude diagram is similar to that observed for two-dimensional simulations

at $Re = 250$, $m^*\zeta = 0.127$ — see Figure 2 in Blackburn & Henderson (1996), allowing for variation in T_n as opposed to U , which reverses orientation on the abscissa.

Of the three response branches observed in the two-dimensional results, only the lowest amplitude branch was associated with conventional periodic Kármán-mode vortex shedding (with period close to that for a fixed cylinder at corresponding Reynolds number). On the high-response branch, the time trace of response amplitude was very nearly sinusoidal for all simulations, with a frequency near the structural natural frequency; however, only for the very highest amplitude did the lift-response phase plane plot approach a closed limit cycle with periodic vortex shedding. In this case, however, the wake, although periodic, did not exhibit Kármán-mode shedding — see related unconventional but periodic wake modes presented in Blackburn & Henderson (1999). Another significant feature of results on this branch is that they all possessed a time-average wake that was asymmetric about the cylinder centreline, with a time-mean coefficient of lift. On the low StV_r branch with moderate response amplitudes, peak values of both the cross-flow response and force varied significantly over long time scales.

5. FORCES AND CROSS-FLOW RESPONSE

In this section, we present an analysis of force and displacement time-series from the three-dimensional simulation at $StV_r = 1.33$, obtained after sufficient simulation time had elapsed for these to approach a statistically steady state. Results collected over 20 motion cycles are presented — this simulation was also used to collect the phase-averaged results to be described in Section 6.

Figure 4 shows time-series of coefficients of drag and lift, and also of dimensionless cross-flow response amplitude $\alpha = y(t)/D$, presented as functions of normalized time t/T_n .

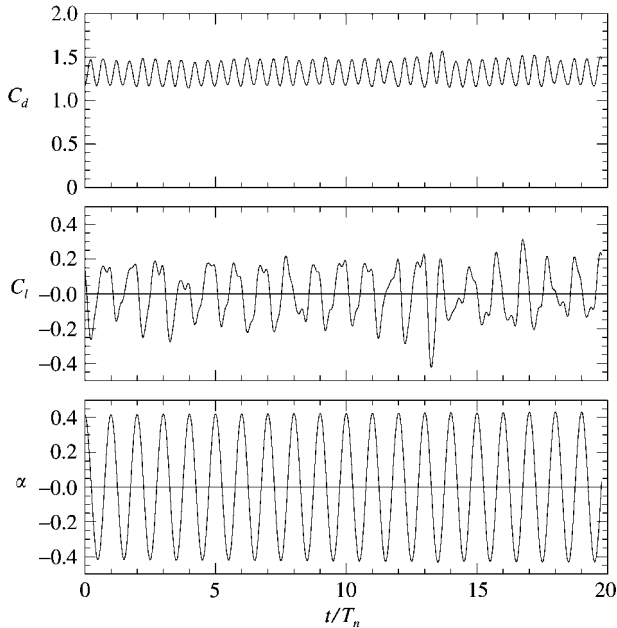


Figure 4. Time-series of coefficients of drag and lift (C_d , C_l), and dimensionless response amplitude α for the three-dimensional simulation at $StV_r = 1.33$.

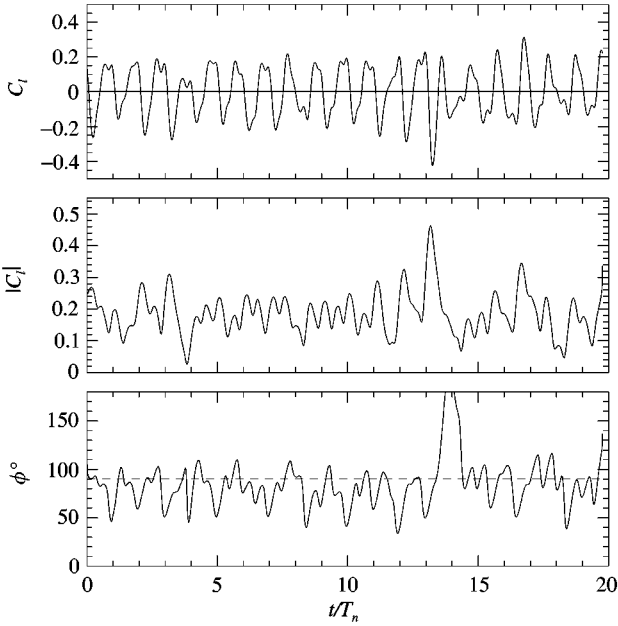


Figure 5. Time-series of lift coefficient, its instantaneous magnitude and phase angle in relation to cross-flow displacement for the three-dimensional simulations.

The time-mean coefficient of drag, $\bar{C}_d = 1.32$, and the standard deviation of coefficient of lift $C_l = 0.14$. Note the typical “double-peaked” nature of the C_l waveform. Despite the quite large variability in the lift force, the cross-flow response stayed nearly sinusoidal in form, as the lift force magnitude is relatively small in comparison to the mechanical restoring force for the spring-mounted cylinder.

Since simulated damping forces are present, there must on average be work done on the cylinder by the lift force; for this to be true the time-average phase angle between the lift force and cylinder displacement must lie in the range 0 – 180° . In Figure 5, we present time series of the coefficient of lift, together with its instantaneous magnitude and phase angle in relation to cross-flow displacement, computed using the Hilbert transform (Schumm *et al.* 1994; Blackburn & Melbourne 1997). Apart from a single large excursion near $t/T_n = 14$, the phase angle ϕ remained near 90° , with average value $\bar{\phi} = 84^\circ$.

The average work done on the cylinder by lift forces can also be assessed by examining the area enclosed by a phase-plane plot of C_l versus α (Blackburn & Henderson 1999). In Figure 6(a) we show the phase-plane plot for the data presented in Figure 4. On the C_l versus α trajectory, the sense of traverse is clockwise, as it must be for a transfer of energy from the fluid to the cylinder. The two largest excursions from the average trajectory correspond to the largest positive and negative peaks in the C_l time-series, while the wave-shaped form of the average trajectory is related to the double-peaked characteristic of the C_l time-series. In Figure 6(b) we present the phase-plane plot from the related set of experiments described in Govardhan & Williamson (2000): this set of data is for $StV_r = 1.27$, and it can be seen to have a similar nature (and peak amplitude) to that for the current simulations, although the form is more stable over time — however, since the mass-damping value is higher than for the present work, the enclosed area in Figure 6(b) is greater than that in Figure 6(a).



Figure 7. Instantaneous isosurfaces of pressure (predominant alignment spanwise) and streamwise vorticity (predominantly streamwise) from three-dimensional simulation. The cylinder is upstream at left.

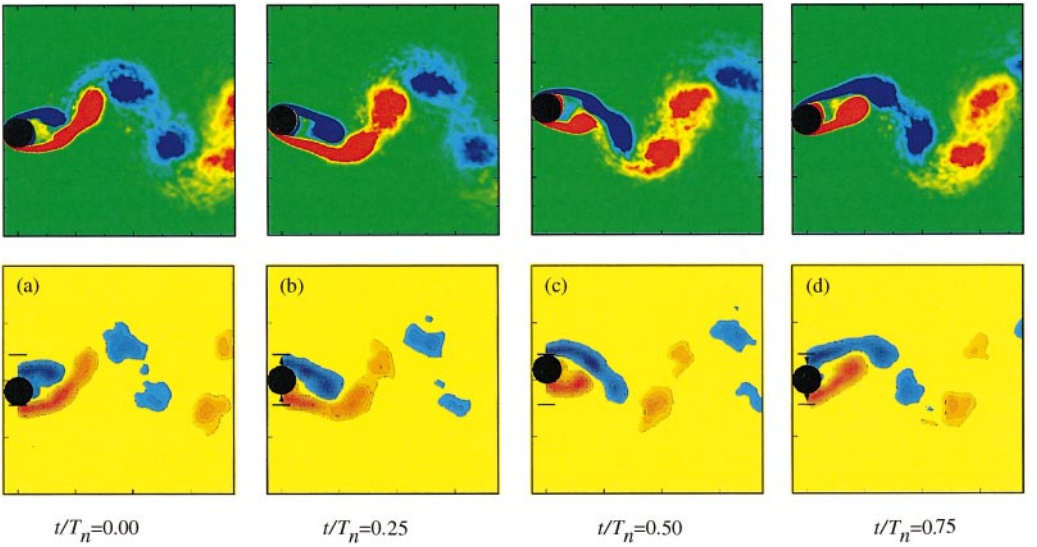


Figure 8. Phase and spanwise average contours of spanwise vorticity for four phases of the cylinder motion cycle (upper plots), compared to (lower) similar (two-dimensional) phase averages from experiments at a somewhat higher Reynolds number (Govardhan & Williamson 2000).

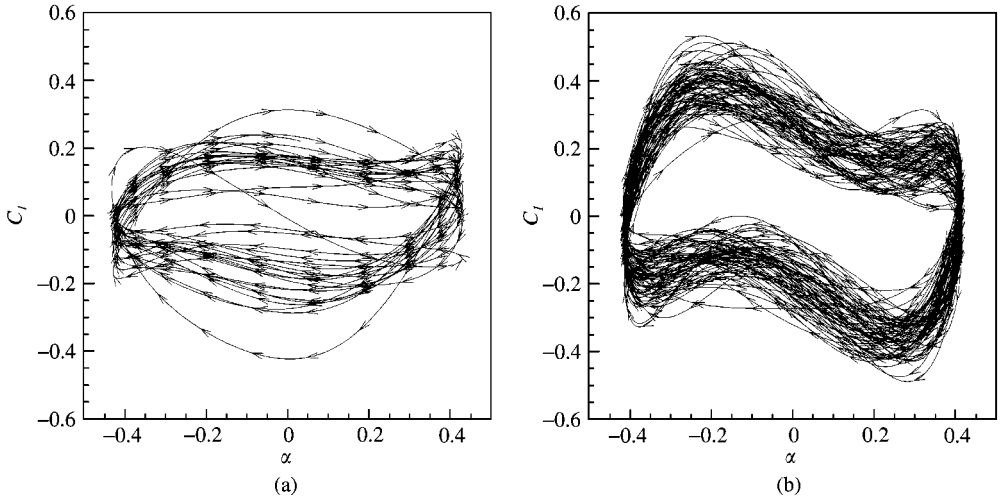


Figure 6. Phase-plane plot of C_l versus α ; the area enclosed by the average trajectory is representative of the average work transfer per motion cycle between the fluid and the cylinder. (a) Data from three-dimensional simulation at $StV_r = 1.33$; (b) data from a set of experiments at higher Reynolds number but $StV_r = 1.27$ with a similar response amplitude (Govardhan & Williamson 2000).

6. VORTEX SHEDDING MODES

Now we turn to an examination of the topology of the wake for the three-dimensional simulation at $StV_r = 1.33$. In Figure 7 we show a plot of instantaneous isosurfaces of pressure and streamwise vorticity. Note that, especially in the near-wake, there is intense turbulent activity, which is particularly evident in the vorticity isosurfaces — isosurfaces of spanwise directed vorticity, or of vorticity magnitude, show similar disorganization.

In order to find the coherent structure of the near-wake, we have used a phase-averaging approach related to that adopted by Cantwell & Coles (1983). Estimates of the ensemble-average velocity field are computed from averages taken at four phases of the motion cycle — since the motion is very nearly periodic it is appropriate to use the cross-flow motion amplitude as a conditioning signal. From the simulations used to produce the data shown in Figure 4 we have collected 20 velocity field averages at each of the four phases: $t/T_n = 0.0$ (maximum negative displacement), $t/T_n = 0.25$ (maximum positive velocity), etc. For each of these four average fields we compute the vorticity, then its spanwise average.

Contours of span- and phase-averaged spanwise vorticity for each of the four phases are presented in Figure 8. For purposes of comparison, we have also shown contours of phase-averaged spanwise vorticity computed from the DPIV data of Govardhan & Williamson (2000), measured at $StV_r = 1.27$ — the overall similarity of these two sets of results is immediately apparent despite some differences in detail. It is evident that in each half motion cycle, the shear layer from one side of the cylinder rolls up into two distinct concentrations of vorticity as it leaves the near-wake region. As they evolve downstream, the four regions of concentrated vorticity form into pairs of counter-rotating vortex couples, one on each side of the wake.

7. DISCUSSION AND CONCLUSIONS

This work represents the first direct comparison between numerical and physical experiments in vortex-induced vibration, in which both fluid and mechanical dynamic parameters

have been matched. There have been some operational problems on both sides, related to the difficulties in obtaining high Reynolds number values in the simulations, on the one hand, and low values in experiments, on the other; however, the results are encouraging.

A significant outcome is that it appears that, at least in the absence of a turbulence model, two-dimensional simulations are inadequate for the task of predicting the full nature both of the response envelope and of vortex shedding mechanics, even at these low Reynolds numbers. This finding is likely to hold both for free and forced cylinder oscillations. Whether the difference between two- and three-dimensional dynamics is caused by effects in the very near-wake produced by turbulence in the vortex formation region, or perhaps by feedback from changed conditions further downstream as the streamwise roller structures evident in Figure 7 enhance the transfer of free-stream momentum into the centre of the wake, is a matter open for further investigation.

Another significant outcome is that, for the first time in a set of simulation results, we have clear evidence (Figure 8) of the 2P shedding mode first reported in Williamson & Roshko (1988). The double-peaked form of the lift time-series exhibited in Figures 4 and 5 and the characteristic shape of the average C_l versus α trajectory shown in Figure 6 are both likely to be related to the shedding of four concentrated regions of vorticity per motion cycle, although the relationship remains to be examined in detail. On the evidence of the smaller excursions from the average trajectory shown in Figure 6(b), when compared to those in Figure 6(a), it appears that the 2P shedding mode may become better established as the Reynolds number increases.

REFERENCES

- BLACKBURN, H. M. & HENDERSON, R. D. 1996 Lock-in behaviour in simulated vortex-induced vibration. *Experimental Thermal and Fluid Science* **12**, 184–189.
- BLACKBURN, H. M. & HENDERSON, R. D. 1999 A study of two-dimensional flow past an oscillating cylinder. *Journal of Fluid Mechanics* **385**, 255–286.
- BLACKBURN, H. M. & KARNIADAKIS, G. E. 1993 Two- and three-dimensional simulations of vortex-induced vibration of a circular cylinder. In *Proceedings of the Third (1993) International Offshore and Polar Engineering Conference, Singapore*, Vol. III, pp. 715–720, Golden, CA, U.S.A.: ISOPE.
- BLACKBURN, H. M. & MELBOURNE, W. H. 1997 Sectional lift forces for an oscillating cylinder in smooth and turbulent flows. *Journal of Fluids and Structures* **11**, 413–431.
- CANTWELL, B. J. & COLES, D. 1983 An experimental study of entrainment and transport in the turbulent near wake of a circular cylinder. *Journal of Fluid Mechanics* **136**, 321–374.
- FENG, C. C. 1968 The measurement of vortex-induced effects in flow past stationary and oscillating circular and D-section cylinders. Master's Thesis, University of British Columbia, Vancouver, BC, Canada.
- GOVARDHAN, R. N. & WILLIAMSON, C. H. K. 2001 Mean and fluctuating velocity fields in the wake of a freely vibrating cylinder. *Journal of Fluids and Structures* **15**, xxx–xxx.
- GOVARDHAN, R. & WILLIAMSON, C. H. K. 2000 Modes of vortex formation and frequency response of a freely vibrating cylinder. *Journal of Fluid Mechanics* **420**, 85–130.
- KHALAK, A. & WILLIAMSON, C. H. K. 1997 Fluid forces and dynamics of a hydroelastic structure with very low mass and damping. *Journal of Fluids and Structures* **11**, 973–982.
- KHALAK, A. & WILLIAMSON, C. H. K. 1999 Motions, forces and mode transitions in vortex-induced vibrations at low mass-damping. *Journal of Fluids and Structures* **13**, 813–851.
- NORBERG, C. 1994 An experimental investigation of the flow around a circular cylinder: influence of aspect ratio. *Journal of Fluid Mechanics* **258**, 287–316.
- SCHUMM, M., BERGER, E. & MONKEWITZ, P. A. 1994 Self-excited oscillations in the wake of two-dimensional bluff bodies and their control. *Journal of Fluid Mechanics* **271**, 17–53.
- WILLIAMSON, C. H. K. & ROSHKO, A. 1988 Vortex formation in the wake of an oscillating cylinder. *Journal of Fluids and Structures* **2**, 355–381.